A&A 677, A21 (2023)
https://doi.org/10.1051/0004-6361/202346196

Astronomy & Astrophysics

Investigating *Gaia* EDR3 parallax systematics using asteroseismology of Cool Giant Stars observed by *Kepler*, K2, and TESS

I. Asteroseismic distances to 12 500 red-giant stars⋆

S. Khan[1], A. Miglio[2,3,4], E. Willett[4], B. Mosser[5], Y. P. Elsworth[4], R. I. Anderson[1], L. Girardi[6], K. Belkacem[5], A. G. A. Brown[7], T. Cantat-Gaudin[8], L. Casagrande[9,10], G. Clementini[3], and A. Vallenari[6]

[1] Institute of Physics, Laboratory of Astrophysics, École Polytechnique Fédérale de Lausanne (EPFL), Observatoire de Sauverny, 1290 Versoix, Switzerland
e-mail: saniya.khan@epfl.ch
[2] Dipartimento di Fisica e Astronomia, Universitä degli Studi di Bologna, Via Gobetti 93/2, 40129 Bologna, Italy
[3] INAF – Osservatorio di Astrofisica e Scienza dello Spazio di Bologna, Via Gobetti 93/3, 40129 Bologna, Italy
[4] School of Physics and Astronomy, University of Birmingham, Edgbaston, Birmingham B15 2TT, UK
[5] LESIA, Observatoire de Paris, PSL Research University, CNRS, Sorbonne Université, Université Paris-Cité, 92195 Meudon, France
[6] INAF – Osservatorio Astronomico di Padova, Vicolo dell'Osservatorio 5, 35122 Padova, Italy
[7] Leiden Observatory, Leiden University, Niels Bohrweg 2, 2333 CA Leiden, The Netherlands
[8] Max-Planck-Institut für Astronomie, Königstuhl 17, 69117 Heidelberg, Germany
[9] Research School of Astronomy and Astrophysics, The Australian National University, Canberra ACT 2611, Australia
[10] ARC Centre of Excellence for All Sky Astrophysics in 3 Dimensions (ASTRO 3D), Stromlo, Australia

Received 20 February 2023 / Accepted 10 April 2023

ABSTRACT

Gaia EDR3 has provided unprecedented data that has generated a great deal of interest in the astrophysical community, even though systematics affect the reported parallaxes at the level of ∼10 µas. Independent distance measurements are available from asteroseismology of red-giant stars with measurable parallaxes, whose magnitude and colour ranges more closely reflect those of other stars of interest. In this paper we determine distances to nearly 12 500 red-giant-branch and red clump stars observed by *Kepler*, K2, and TESS. This was done via a grid-based modelling method, where global asteroseismic observables, and constraints on the photospheric chemical composition and on the unreddened photometry are used as observational inputs. This large catalogue of asteroseismic distances allows us to provide a first comparison with *Gaia* EDR3 parallaxes. Offset values estimated with asteroseismology show no clear trend with ecliptic latitude or magnitude, and the trend whereby they increase (in absolute terms) as we move towards redder colours is dominated by the brightest stars. The correction model proposed by Lindegren et al. (2021a) is not suitable for all the fields considered in this study. We find a good agreement between asteroseismic results and model predictions of the red clump magnitude. We discuss possible trends with the *Gaia* scan law statistics, and show that two magnitude regimes exist where either asteroseismology or *Gaia* provides the best precision in parallax.

Key words. asteroseismology – astrometry – parallaxes – stars: distances – stars: low-mass – stars: oscillations

1. Introduction

In December 2020, the early third intermediate data release of *Gaia* (*Gaia* EDR3; Gaia Collaboration 2021) was published, with an updated source list, astrometry, and broad-band photometry in the G, G_{BP}, and G_{RP} bands. This release represents a significant improvement in both the precision and accuracy of the astrometry and photometry, with respect to *Gaia* DR2. While quasars yielded a median parallax of −29 µas in DR2, this is now reduced to about −17 µas in *Gaia* EDR3, with variations at a level of ∼10 µas depending on position, magnitude, and colour (Lindegren et al. 2021b).

With the EDR3 release, Lindegren et al. (2021a, hereafter L21) proposed two offset functions, $Z_5(G, \nu_{\rm eff}, \beta)$ and $Z_6(G, \hat{\nu}_{\rm eff}, \beta)$, applicable to five- and six-parameter astrometric solutions, respectively, that give an estimate of the systematics in the parallax measurement as a function of the G-band magnitude, effective wavenumber $\nu_{\rm eff}$ or pseudo-colour $\hat{\nu}_{\rm eff}$, and ecliptic latitude β. Their zero-point correction model is based on quasars and is complemented with indirect methods involving physical binaries and stars in the Large Magellanic Cloud[1].

⋆ Catalogues described in Appendix A are only available at the CDS via anonymous ftp to cdsarc.cds.unistra.fr (130.79.128.5) or via https://cdsarc.cds.unistra.fr/viz-bin/cat/J/A+A/677/A21

[1] Python implementations of both functions are available on the *Gaia* web pages: https://www.cosmos.esa.int/web/gaia/edr3-code

Table 1. Overview of the properties of the different datasets.

Fields	Baseline	G	$\nu_{\rm eff}$ (μm^{-1})
Kepler	4 yr	[9, 13]	[1.4, 1.5]
K2	80 days	[9, 15]	[1.35, 1.5]
TESS-SCVZ	1 yr	[9, 11]	[1.4, 1.5]

Notes. Observation length, range in G magnitude and in $\nu_{\rm eff}$ are given.

Despite the availability of this correction, L21 still encourage users of *Gaia* EDR3 data to derive their own zero-point estimates whenever possible. Some studies dedicated to the comparison between EDR3 parallaxes and independent measurements have found that the inclusion of the L21 offset could lead to an overcorrection of the parallaxes. All the values reported below give the difference between the corrected EDR3 parallaxes and the other measurements. Hence, positive values correspond to an overcorrection, as a result of applying the L21 values[2]. This includes samples based on classical Cepheids ($+14 \pm 5\,\mu$as, Riess et al. 2021; $+18 \pm 5\,\mu$as and $+22 \pm 3\,\mu$as, based on NIR HST and optical *Gaia* bands, respectively, Cruz Reyes & Anderson 2023; $+22 \pm 4\,\mu$as, Molinaro et al. 2023) and RR Lyrae stars ($+22 \pm 2\,\mu$as; Bhardwaj et al. 2021). Even so, there are other studies that did not report this overestimation of the parallax zero point, as can be seen from eclipsing binaries ($-15 \pm 18\,\mu$as; Stassun & Torres 2021), red clump stars ($+4.04\,\mu$as, the uncertainty is not reported; Huang et al. 2021), and WUMa-type eclipsing binary systems ($+4.2 \pm 0.5\,\mu$as; Ren et al. 2021).

Following on from our *Gaia* DR2 study (Khan et al. 2019, hereafter K19), we extend our catalogue of distances using asteroseismic data in the *Kepler*, K2, and TESS southern continuous viewing zone (TESS-SCVZ) fields, allowing for a first comparison with *Gaia* EDR3. The asteroseismic and spectroscopic surveys used are briefly described in Sect. 2. The method for estimating asteroseismology-based parallaxes is introduced in Sect. 3. Section 4 presents our parallax zero-point results for *Kepler*, K2, and TESS separately, and provides a first discussion of global trends seen in ecliptic latitude, magnitude, and effective wavenumber. In Sect. 5 we discuss the magnitude of the red clump as an independent validation of the method, the impact of *Gaia* scanning law statistics for K2, and the existence of two regimes in magnitude where either the precision of asteroseismology or *Gaia* dominates. Our conclusions are reported in Sect. 6.

2. Observational framework

Our sample is divided into three main parts, summarised in Table 1, and the location of the various fields is illustrated in Fig. 1. The full datasets with asteroseismic, spectroscopic, and astrometric information are provided along with the paper, and details about the columns are given in Appendix A.

2.1. Asteroseismic information

We first have first-ascent red-giant-branch (RGB) stars and red clump (RC) stars observed by *Kepler* (Borucki et al. 2010), for which the observation length is the longest: four years. The second part of our sample consists of red giants observed by K2, *Kepler*'s follow-up mission (Howell et al. 2014). Compared to the two campaigns analysed in K19, we now have data available for 17 campaigns: C01-08, C10-18. The observations of K2 campaigns have a much shorter duration of 80 days. We further analysed very bright ($G < 11$) red-giant stars in the TESS-SCVZ (Ricker et al. 2015). The TESS full-frame images, from which the asteroseismic data are extracted, are based on one year of observations.

For all three surveys, we use the frequency of maximum oscillation power $\nu_{\rm max}$ and the average large frequency spacing $\langle\Delta\nu\rangle$, and consider two different asteroseismic pipelines: Mosser & Appourchaux (2009, hereafter MA09) and Elsworth et al. (2020, hereafter E20). We keep stars for which both pipelines return a $\nu_{\rm max}$ value in the range [15, 200] μHz. Beyond these limits the $\nu_{\rm max}$ estimates are more uncertain and can deviate significantly between MA09 and E20.

2.2. Spectroscopic information

For K2, two different surveys are considered for constraints on the photospheric chemical composition (i.e. $T_{\rm eff}$ and [Fe/H], and, if available, [α/Fe]): APOGEE DR17 with near-infrared (NIR) all-sky spectroscopic observations and a resolution of $R \sim 22\,500$ (Abdurro'uf et al. 2022), and GALAH DR3 with southern hemisphere spectroscopic observations in the optical/NIR and $R \sim 28\,000$ (Buder et al. 2021). For *Kepler* and TESS, we only use APOGEE constraints. Additional flags are also applied following recommendations specific to each spectroscopic survey[3]. Another survey that could be considered is the all-sky *Gaia* DR3 GSP-Spec observing in the NIR and with $R \sim 11\,500$ (Recio-Blanco et al. 2023), but this is beyond the scope of this work.

3. Asteroseismic parallaxes

Asteroseismic parallaxes are estimated with the Bayesian tool `PARAM` (Rodrigues et al. 2017). For a given set of observational inputs: $\nu_{\rm max}$, $\langle\Delta\nu\rangle$, $T_{\rm eff}$, log g, [Fe/H], and [α/Fe] (when available), as well as photometric measurements, the code determines the best-fitting stellar parameters by searching amongst a grid of models. The outputs are given in the form of probability density functions, from which the median and 68% credible intervals lead to the final parameters of interest and their uncertainties. We refer the reader to Miglio et al. (2021) for a more extensive discussion of the importance of uncertainties related to stellar models.

In particular, asteroseismic and spectroscopic constraints are combined to derive absolute magnitudes in the different passbands using bolometric corrections from Girardi et al. (2002). Extinction coefficients are computed by adopting the reddening laws of Cardelli et al. (1989) and O'Donnell (1994) with $R_V = 3.1$. It is then assumed that extinctions in all filters A_λ are related by a single interstellar extinction curve expressed in terms of its V-band value, that is $A_\lambda(A_V)$. The total extinction A_V and the distance d can then be derived simultaneously. Parallaxes are obtained by inverting the said distances (with a relative uncertainty below $\sim 5\%$), and the error on the distance is propagated to obtain the uncertainty on the parallax. We provide a comparison with *Gaia* DR3 GSP-Phot distances in Appendix B.

[2] In this work we define the residual parallax offset as $\Delta\varpi_{\rm corr} = (\varpi_{\rm EDR3} - Z_5) - \varpi_{\rm other}$, while some of the studies mentioned define it with the opposite sign: $\Delta\varpi_{\rm corr} = \varpi_{\rm other} - (\varpi_{\rm EDR3} - Z_5)$.

[3] We used the `STAR_WARN` and `STAR_BAD` flags to clean the APOGEE sample (`https://www.sdss.org/dr17/irspec/parameters/`) and `flag_sp == 0`, `flag_fe_h == 0`, `flag_alpha_fe == 0` for the GALAH sample (`https://www.galah-survey.org/dr3/flags/`).

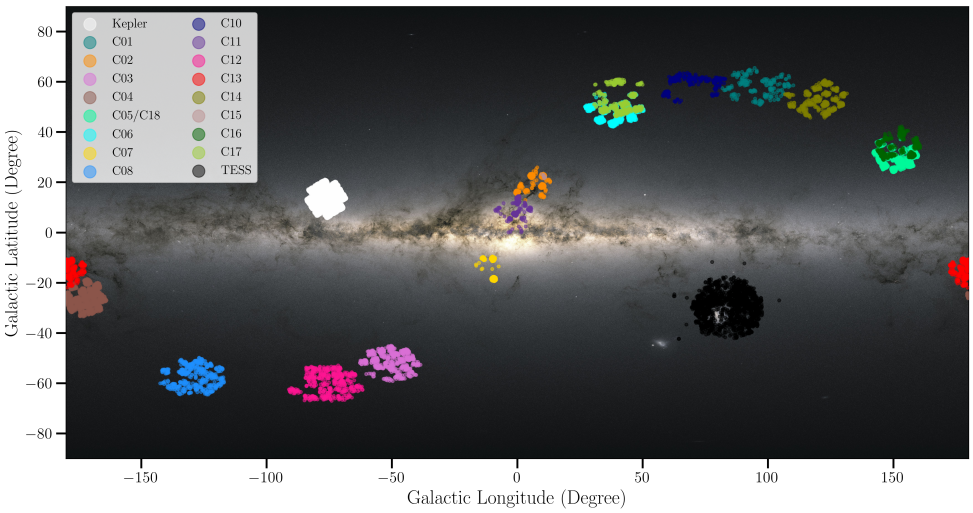

Fig. 1. Skymap in Galactic coordinates. Shown are the location and coverage resulting from the crossmatch between the various asteroseismic fields considered in this study and APOGEE DR17. This figure has been generated using the `Python` package `mw-plot` (`milkyway-plot.readthedocs.io`). The background image comes from ESA/*Gaia*/DPAC.

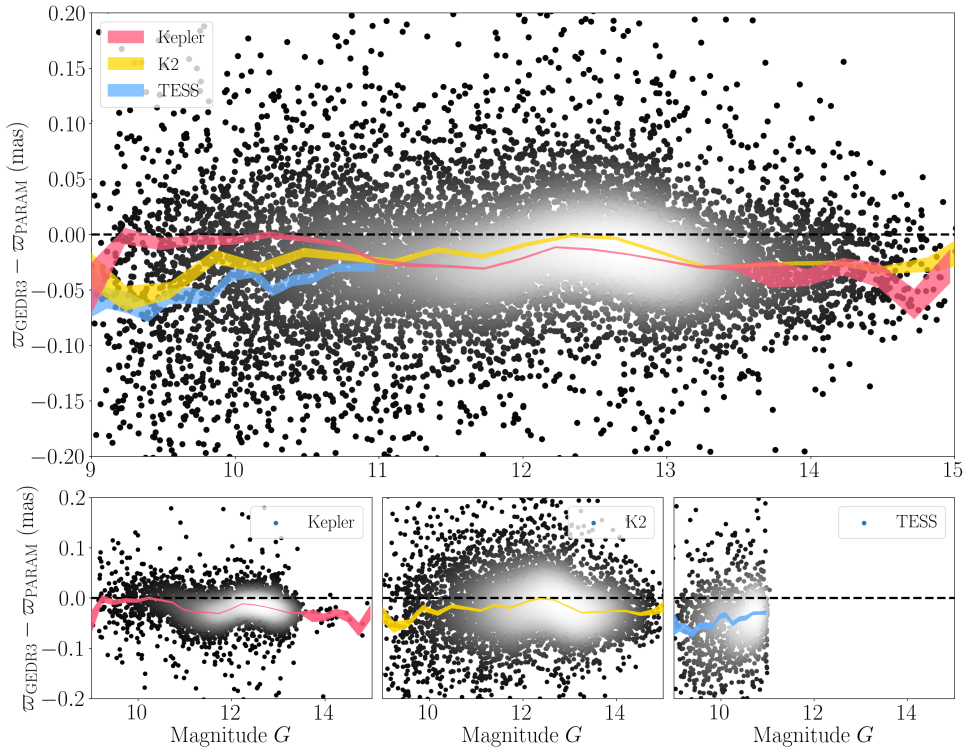

Fig. 2. Parallax difference $\varpi_{EDR3} - \varpi_{PARAM}$ as a function of G magnitude for the full sample (top), *Kepler* (bottom left), K2 (bottom middle), and TESS (bottom right), using E20 and APOGEE DR17. The colour scale indicates the density of stars, increasing from black to white. The red, yellow, and blue shaded areas show the median parallax difference binned by magnitude for *Kepler*, K2, and TESS, respectively.

4. First comparison to *Gaia* EDR3 parallaxes

To simplify the discussion and figures, we focus on one combination of asteroseismic and spectroscopic constraints. For most K2 fields, the offsets measured using the MA09 or E20 seismic observables agree to within a few microarcseconds. For TESS-SCVZ targets, Mackereth et al. (2021) found the $\langle\Delta\nu\rangle$ values returned by the E20 pipeline to be more consistent with individual-mode frequencies (and thus to the method employed in models). Hence, we use the E20 asteroseismic pipeline for all three fields. Systematic differences in the spectroscopic parameters published by different surveys affect our results at the level of 5–10 µas (also partly due to the samples being different). We therefore adopt a single homogeneous spectroscopic dataset (APOGEE DR17) to ensure the greatest precision.

A summary of the parallax zero points derived is given in Table 2, whilst individual offsets for all combinations of seismic and spectroscopic constraints are provided in Appendix C. More detailed checks on how the asteroseismic method and the choice of spectroscopy affect the analysis of *Gaia* systematics will be presented in a forthcoming paper (Khan et al., in prep.).

4.1. Separate analyses for Kepler, K2, and TESS

In the following, our results are based on five-parameter astrometric solutions only. We estimate the parallax offset for each field, before and after applying L21 corrections to *Gaia* parallaxes, and study potential trends with asteroseismic, spectroscopic, and photometric parameters. We had initially compared our results with the Zinn (2021) analysis of *Kepler* targets. However, the results are not directly comparable because versions 0.0.1 and 0.0.2 of the *Gaia*-provided Python implementation of the correction `zero_point` incorrectly applied the ecliptic latitude term.

Table 2. Summary of the different combinations of asteroseismic and spectroscopic constraints used in this study for the fields considered: *Kepler*, K2 (C01-08, C10-18), and TESS-SCVZ.

Fields	Seismo.	Spectro.	N	$\langle\Delta\varpi\rangle$ (μas)	$\langle\Delta\varpi_{\rm corr}\rangle$ (μas)	Full range	Full range (corr.)
Kepler	MA09	APOGEE DR17	4687	-32 ± 0.4	-12 ± 0.4	–	–
	E20	–	–	-20 ± 0.3	-0.4 ± 0.3	–	–
K2	MA09	APOGEE DR17	7024	-18^{+9}_{-7}	$+15^{+6}_{-7}$	[−43, +2]	[−6, +33]
	E20	–	–	-18^{+12}_{-6}	$+14^{+12}_{-7}$	[−39, +1]	[−4, +32]
	MA09	GALAH DR3	5919	-19^{+8}_{-6}	$+13^{+11}_{-6}$	[−68, +4]	[−41, +32]
	E20	–	–	-19^{+8}_{-7}	$+14^{+12}_{-8}$	[−70, +15]	[−45, +43]
TESS-SCVZ	MA09	APOGEE DR17	1253	-23 ± 1.2	-15 ± 1.2	–	–
	E20	–	–	-41 ± 1.4	-33 ± 1.4	–	–

Notes. The median parallax offsets obtained before applying L21 corrections ($\Delta\varpi = \varpi_{\rm EDR3} - \varpi_{\rm PARAM}$) and after ($\Delta\varpi_{\rm corr} = \varpi_{\rm EDR3,corr} - \varpi_{\rm PARAM}$) are indicated. For K2, the median offset is calculated considering the 17 campaigns together, and the uncertainty quoted corresponds to the 16th and 84th percentiles. In addition, the full range with the minimum and maximum offsets measured for K2 fields is also given.

We investigate the parallax difference $\Delta\varpi = \varpi_{\rm EDR3} - \varpi_{\rm PARAM}$ as a function of G, and verify that $\Delta\varpi$ is negative for all fields, in the sense that *Gaia* parallaxes are smaller (Fig. 2). We apply the same analysis as in K19 on the *Kepler* sample, but this time with *Gaia* EDR3 parallaxes and updated APOGEE constraints. The quantity $\Delta\varpi$ shows fairly flat trends as a function of the ecliptic latitude, the effective wavenumber, the frequency of maximum oscillation, the mass inferred from `PARAM`, and the metallicity, but not for the G magnitude, which displays a non-linear feature (see bottom left panel of Fig. 2). This relation with G is expected due to changes in the gating scheme or in the window size (see Fig. 17 in Fabricius et al. 2021). Despite the larger scatter and a higher proportion of fainter stars compared to *Kepler*, we also observe a non-linear trend as a function of G if we combine all K2 fields together, which have an ecliptic latitude near zero (see bottom middle panel of Fig. 2). However, our TESS-SCVZ sample is too bright for us to see this trend.

Figure D.1 is similar to Fig. 2, but shows instead the parallax offset residuals $\Delta\varpi_{\rm corr} = \varpi_{\rm EDR3,corr} - \varpi_{\rm PARAM}$, with Z_5-corrected *Gaia* EDR3 parallaxes. This removes the non-linear trend with G. It is also clear from Fig. D.1 that L21 corrections underestimate the parallax offset in the case of TESS, and overestimate it for the K2 fields. However, in *Kepler* the residual parallax offset gets very close to zero. This suggests that L21 corrections are not universally suited for different types of sources, spanning a wide range of positions, magnitudes, and colours.

For some of the K2 campaigns (and independently of the spectroscopy used), we note a significant trend of the parallax difference with the stellar mass. As we do not observe such a trend with mass for *Kepler* and TESS, we suspect that it could be related to, for instance, different noise levels in the various K2 campaigns. We tried using scaling relations to compute the mass and the asteroseismic parallax instead of `PARAM`, tested different asteroseismic pipelines and spectroscopic surveys, and removed high $\nu_{\rm max}$ stars. Unfortunately, none of these made a difference and this is still being investigated (by BM and YE) as it might directly be related to the accuracy of seismically inferred parameters.

4.2. Global picture

In Fig. 3 we show the offset estimates $\Delta\varpi$ suggested from the difference between the uncorrected *Gaia* EDR3 and `PARAM` parallaxes in the *Kepler*, the individual K2 campaigns, and the TESS-SCVZ fields. We analyse the relation between the parallax zero point and the ecliptic latitude β, the G magnitude, and the effective wavenumber $\nu_{\rm eff}$, which are the three parameters constituting the L21 correction model.

We first note that the offsets measured from asteroseismology are either close to zero or negative, and lie (at most) a few tens of μas away from the zero point suggested by quasars (~ -17 μas). All the K2 campaigns have a similar $\sin\beta$, close to zero, which is expected as the K2 survey observed solar-like oscillators all along the ecliptic.

For individual K2 campaigns, the parallax difference also follows a non-linear relationship with G, in line with what is discussed in Sect. 4.1. The bottom panel of Fig. 3 suggests that the parallax difference becomes more negative as we go towards lower $\nu_{\rm eff}$, that is redder colours. This is also apparent for $\nu_{\rm eff} \lesssim 1.40$, where we have fewer campaigns. One should keep in mind, however, that this trend is dominated by bright stars, for which other caveats exist (see e.g. Sect. 5.3), which tend to drag the parallax difference towards substantially negative values (as can be seen from the middle panel of Fig. 3).

5. Discussion

5.1. Magnitude of the red clump

As a way to validate our findings, we also analyse the information provided by the magnitude of the red clump. In Fig. 4 we show different estimates of the absolute magnitude of the clump as a function of the galactic latitude b. The first estimate is based on the K_s-band absolute magnitude computed by `PARAM`, which is thus representative of our asteroseismic samples. For the other two estimates, we select *Gaia* EDR3 sources centred around the coordinates of each field and with $1 < G < 15$: one estimate is calculated with the inverted *Gaia* uncorrected parallaxes and the other with corrected parallaxes (using the L21 correction model). In order to be able to safely use inverted parallaxes, we restrict our samples to *Gaia* sources with a relative parallax uncertainty lower than 10%. Extinctions are calculated with the combined map (Marshall et al. 2006; Green et al. 2019; Drimmel et al. 2003) from `mwdust`[4] (Bovy et al. 2016),

[4] https://github.com/jobovy/mwdust

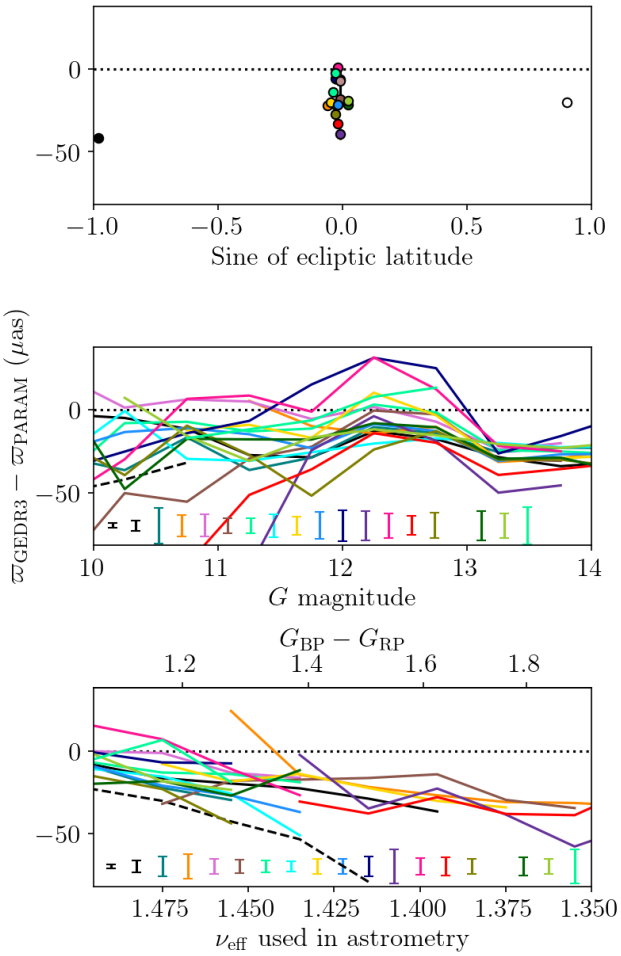

Fig. 3. Global trends for our parallax zero points as a function of the three quantities defining the L21 correction. Top: Median parallax offsets estimated from asteroseismology (E20+APOGEE) as a function of the sine of ecliptic latitude. *Kepler* and TESS are plotted as white and black symbols, respectively. The coloured symbols correspond to the various K2 fields, and follow the colour scheme adopted in Fig. 1. Middle and bottom: Median parallax difference binned by G magnitude (middle) and effective wavenumber (bottom). *Kepler* and TESS are plotted as black solid and dashed lines, respectively. The median uncertainty on the parallax difference is shown in the lower part of each panel. C15 does not appear in the two bottom panels as there are not enough stars to bin in G and $\nu_{\rm eff}$.

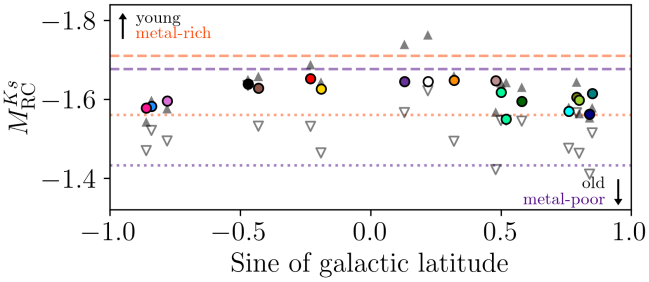

Fig. 4. Magnitude of the red clump in K_s band estimated from our asteroseismic sample (circles, same colour scheme as in Fig. 1), and *Gaia* EDR3 samples before applying L21 corrections (filled triangles) and after (open triangles), as a function of the sine of the galactic latitude. The lines show predictions from modelling: purple and orange respectively for a metal-poor (−0.4 dex) and metal-rich model (+0.2 dex); dashed and dotted respectively for a young (5 Gyr) and old model (12 Gyr; see Fig. 8 in Girardi 2016). These values were chosen to be representative of the lower and upper bounds of the metallicity and age distributions in the asteroseismic fields.

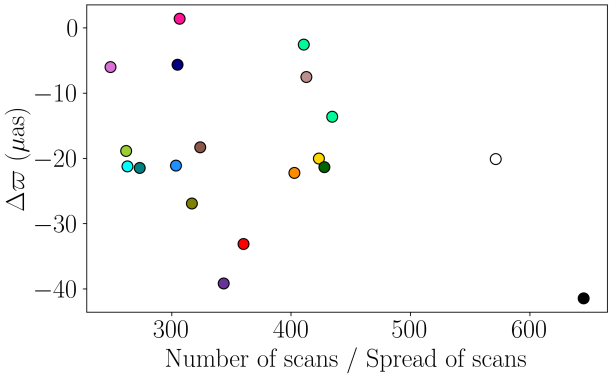

Fig. 5. Parallax offset, measured as difference between uncorrected *Gaia* EDR3 and asteroseismic parallaxes as a function of number of scans over spread of scans. A low value suggests fewer scans clustered at one time of the year, and hence an astrometry of lesser quality, while a higher value corresponds to a greater number of scans better separated in time. The colour scheme is the same as in Fig. 1.

and should only have a minor effect on the current analysis as we are working with K_s-band magnitudes. For each dataset we then compute the mode of the magnitude of the red clump using a kernel density estimation with a fixed bandwidth (equal to 0.1) on the corresponding histogram.

The magnitude of the red clump shows a trend with galactic latitude. Figure 3 of Ren et al. (2021) shows that the parallax offset is observed to be more negative for $\sin b \sim 0$, which could explain why the filled triangles are more luminous in our Fig. 4. On the other hand, a brighter red clump luminosity would result from a younger and more metal-rich population. This trend is visible when using the seismic sample or the *Gaia* EDR3 sample without applying L21 parallax corrections. Instead, the corrected *Gaia* EDR3 sample shows a flat trend, which again supports the idea that the L21 zero-point model is not suitable for every kind of star (see also Sect. 4.1). In addition, results from asteroseismology agree well with model predictions (see e.g. Girardi 2016).

5.2. Impact of Gaia scanning law statistics for K2

We look into whether the spread in parallax zero points suggested by the K2 fields could be related to *Gaia* scan law statistics. For this we extracted both the average number of scans and spread of scans throughout the year for *Gaia* EDR3 (see Fig. 1 of Everall et al. 2021 for the all-sky distribution of these quantities in *Gaia* DR2). The high ecliptic latitude fields, *Kepler* and TESS, show a high number of scans and an important spread of scans. On the other hand, for K2 we find fewer scans that are often concentrated at a single time of the year, which is consistent with the fact that these fields are located unfavourably with respect to the *Gaia* scanning law. As a result, the uncertainty on *Gaia* EDR3 parallaxes is larger for K2 compared to *Kepler* and TESS. Apart from these obvious differences, we do not observe any trend of the parallax offset with the scan law statistics between the various K2 campaigns (see Fig. 5).

5.3. Existence of two magnitude regimes

Figure 6 illustrates the biases arising from asteroseismology or *Gaia*'s point of view as a function of the G-band apparent magnitude. The asteroseismic bias corresponds to a fractional systematic uncertainty in radius and hence in distance, while the

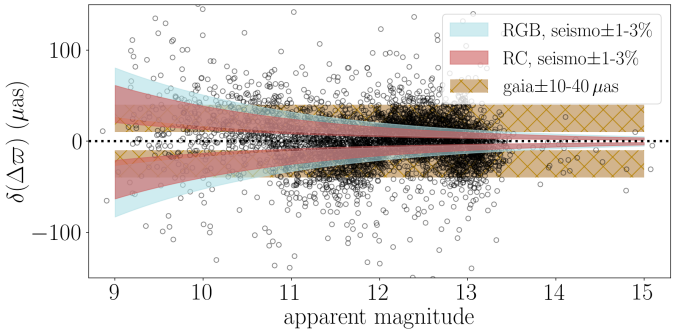

Fig. 6. Bias in the parallax difference as a function of the apparent magnitude. Two mock stars are considered for the asteroseismic bias: a RGB star (blue) and a RC star (red; see text for details). We show the asteroseismic bias that would result from a 1–3% systematic uncertainty in radius. The *Gaia* bias, ±10–40 μas in parallax, is shown as a yellow hatched region. *Kepler* observations are shown in the background after subtracting the mean parallax offset.

Gaia bias would be related to the effect of a systematic (absolute) uncertainty in parallax.

In order to test this we considered two mock stars: a RGB star with $L = 30\,L_\odot$, $T_{\rm eff} = 4630$ K, [Fe/H] = 0.0 dex, $\log g = 2.6$, and a RC star with $L = 50\,L_\odot$, $T_{\rm eff} = 4740$ K, [Fe/H] = 0.0 dex, $\log g = 2.4$. We then estimated the absolute magnitude in the G-band. We considered a range of apparent magnitude values [9, 15], and computed a parallax value for each magnitude. 'Biased' parallaxes are then estimated either by adding a constant to the distance modulus, which would correspond to a fractional uncertainty in radius (asteroseismic bias), or by adding a constant to the parallax itself (*Gaia* bias). For the former we considered a ±1–3% bias in radius, which corresponds to the 16th and 84th percentiles for the *Kepler* dataset, while for the latter we used a range of ±10–40 μas.

We show in Fig. 6 how such biases can affect the estimation of the parallax zero point. The *Kepler* dataset is also shown in the background (after subtracting the mean parallax offset) to see how the order of magnitude of these biases compares with the actual observations. The existence of two regimes becomes quite clear. At the bright end the comparisons in terms of parallax difference are dominated by systematics affecting the seismic parallax; at the faint end the systematics from asteroseismology are much less dominant, and one can potentially expose *Gaia*'s. This division stems from the fact that the fractional uncertainty on asteroseismic distances (or parallaxes) is largely distance independent, but the absolute precision (in pc or mas) is very much distance dependent, so it becomes worse than *Gaia*'s in nearby objects. Similar comparisons of fractional versus constant offset effect as a function of magnitude and other parameters are shown in Figs. 4–7 of Zinn et al. 2019, to which we refer the reader for further discussion.

6. Conclusions

We carried out a follow-up of our 2019 study (Khan et al. 2019) to investigate the *Gaia* EDR3 parallax zero point, for a significantly larger number of asteroseismic fields: *Kepler*, 17 K2 campaigns, and the TESS-SCVZ. Our analysis is similar to that of Zinn (2021) for the *Kepler* field, but goes beyond theirs with the addition of K2 and TESS. In combining results across *Kepler*, K2, and TESS, we have made sure to combine asteroseismic and spectroscopic constraints in a fully homogeneous way. This has the benefit of exploring *Gaia* parallax systematics for the same type of objects but with a wide range of positions over the sky within a single study. A quick comparison of asteroseismic distances with the *Gaia* DR3 GSP-Phot estimates shows that a reasonable agreement is found for objects within 2 kpc.

Firstly, we confirm the positional dependence of the *Gaia* parallax zero point: *Kepler* has an offset of ∼−20 μas, K2 campaigns span a wide range between ∼−39 and +1 μas, and TESS shows an offset of ∼−41 μas when using E20 and APOGEE constraints.

The inclusion of the Lindegren et al. (2021a) zero-point estimates improves the agreement between *Gaia* and asteroseismology in the case of *Kepler* and, to a much lesser extent, TESS. However, in most K2 fields it can significantly overcorrect the parallax difference, sometimes resulting in large positive parallax offsets. This underlines the need to consistently determine the parallax systematics applicable to the sample of interest, taking into account the distributions in position, magnitude, and colour. This overcorrection had already been suggested by previous studies (e.g. Bhardwaj et al. 2021; Riess et al. 2021).

Lastly, in terms of magnitude and colour dependence, we show that asteroseismology provides us with strong constraints on the *Gaia* EDR3 parallax zero point, in ranges that are not necessarily well sampled by L21 corrections. There are no clear trends with the ecliptic latitude or the G magnitude, but the zero-point values tend to increase (in absolute terms) towards redder colours (lower $\nu_{\rm eff}$). Although this trend seems to be dominated by caveats associated with stars at brighter magnitudes. Moreover, we find that seismic-based estimates of the red clump magnitude are consistent with theoretical predictions of $M^{Ks}_{\rm RC}$, and that the inclusion of the L21 offset tends to make the red clump too faint. We do not find any correlation between *Gaia* scan law statistics and parallax offset estimates for the K2 fields. We also use two mock stars to illustrate the existence of two regimes: bright magnitudes, where *Gaia*'s precision is better than asteroseismology's; and faint magnitudes, where we can expose *Gaia*'s limits thanks to seismology's precision.

With this study, we present asteroseismology as a powerful tool for constraining *Gaia* systematics. Red giants come with several benefits: they are single stars with measurable parallaxes and without large-amplitude photometric variations, and thus differ substantially from eclipsing binaries, quasars, RR Lyrae, and Cepheids. Further progress is expected with *Gaia* DR4, which will have improved parallax uncertainties and reduced systematics. In a forthcoming paper we will look in more detail at the uncertainties potentially affecting parallax estimates from asteroseismology and *Gaia*, and investigate how we can define the best sample to study parallax systematics in *Gaia*.

Acknowledgements. This work has made use of data from the European Space Agency (ESA) mission *Gaia* (https://www.cosmos.esa.int/gaia), processed by the *Gaia* Data Processing and Analysis Consortium (DPAC, https://www.cosmos.esa.int/web/gaia/dpac/consortium). Funding for the DPAC has been provided by national institutions, in particular the institutions participating in the *Gaia* Multilateral Agreement. R.I.A. and S.K. are funded by the Swiss National Science Foundation (SNSF) through an Eccellenza Professorial Fellowship (award PCEFP2_194638). A.M. and E.W. acknowledge support from the ERC Consolidator Grant funding scheme (project ASTEROCHRONOMETRY, G.A. n. 772293). This research was supported by the International Space Science Institute (ISSI) in Bern, through ISSI International Team project #490, SHoT: The Stellar Path to the Ho Tension in the *Gaia*, TESS, LSST and JWST Era. We also wish to thank the referee who provided a very positive report.

References

Abdurro'uf, Accetta, K., Aerts, C., et al. 2022, ApJS, 259, 35
Bhardwaj, A., Rejkuba, M., de Grijs, R., et al. 2021, ApJ, 909, 200

Borucki, W. J., Koch, D., Basri, G., et al. 2010, Science, 327, 977
Bovy, J., Rix, H.-W., Green, G. M., Schlafly, E. F., & Finkbeiner, D. P. 2016, ApJ, 818, 130
Buder, S., Sharma, S., Kos, J., et al. 2021, MNRAS, 506, 150
Cardelli, J. A., Clayton, G. C., & Mathis, J. S. 1989, ApJ, 345, 245
Cruz Reyes, M., & Anderson, R. I. 2023, A&A, 672, A85
Drimmel, R., Cabrera-Lavers, A., & López-Corredoira, M. 2003, A&A, 409, 205
Elsworth, Y., Hekker, S., Basu, S., & Davies, G. R. 2017, MNRAS, 466, 3344
Elsworth, Y., Themeßl, N., Hekker, S., & Chaplin, W. 2020, Res. Notes Am. Astron. Soc., 4, 177
Everall, A., Boubert, D., Koposov, S. E., Smith, L., & Holl, B. 2021, MNRAS, 502, 1908
Fabricius, C., Luri, X., Arenou, F., et al. 2021, A&A, 649, A5
Fouesneau, M., Frémat, Y., Andrae, R., et al. 2023, A&A, 674, A28
Gaia Collaboration (Brown, A. G. A., et al.) 2021, A&A, 649, A1
Gaia Collaboration (Vallenari, A., et al.) 2023, A&A, 674, A1
Girardi, L. 2016, ARA&A, 54, 95
Girardi, L., Bertelli, G., Bressan, A., et al. 2002, A&A, 391, 195
Green, G. M., Schlafly, E., Zucker, C., Speagle, J. S., & Finkbeiner, D. 2019, ApJ, 887, 93
Howell, S. B., Sobeck, C., Haas, M., et al. 2014, PASP, 126, 398
Huang, Y., Yuan, H., Beers, T. C., & Zhang, H. 2021, ApJ, 910, L5
Khan, S., Miglio, A., Mosser, B., et al. 2019, A&A, 628, A35
Lindegren, L., Bastian, U., Biermann, M., et al. 2021a, A&A, 649, A4
Lindegren, L., Klioner, S. A., Hernández, J., et al. 2021b, A&A, 649, A2
Mackereth, J. T., Miglio, A., Elsworth, Y., et al. 2021, MNRAS, 502, 1947
Marshall, D. J., Robin, A. C., Reylé, C., Schultheis, M., & Picaud, S. 2006, A&A, 453, 635
Miglio, A., Chiappini, C., Mackereth, J. T., et al. 2021, A&A, 645, A85
Molinaro, R., Ripepi, V., Marconi, M., et al. 2023, MNRAS, 520, 4154
Mosser, B., & Appourchaux, T. 2009, A&A, 508, 877
O'Donnell, J. E. 1994, ApJ, 422, 158
Recio-Blanco, A., de Laverny, P., Palicio, P. A., et al. 2023, A&A, 674, A29
Ren, F., Chen, X., Zhang, H., et al. 2021, ApJ, 911, L20
Ricker, G. R., Winn, J. N., Vanderspek, R., et al. 2015, J. Astron. Telesc. Instrum. Syst., 1, 014003
Riello, M., De Angeli, F., Evans, D. W., et al. 2021, A&A, 649, A3
Riess, A. G., Casertano, S., Yuan, W., et al. 2021, ApJ, 908, L6
Rodrigues, T. S., Bossini, D., Miglio, A., et al. 2017, MNRAS, 467, 1433
Stassun, K. G., & Torres, G. 2021, ApJ, 907, L33
Zinn, J. C. 2021, AJ, 161, 214
Zinn, J. C., Pinsonneault, M. H., Huber, D., & Stello, D. 2019, ApJ, 878, 136

Appendix A: Catalogues of asteroseismic, spectroscopic, and astrometric properties for *Kepler*, K2, and TESS red giants

Table A.1. Description of the columns used in the catalogues we release in this work.

Column Identifier	Description	Units
KIC/K2_ID/TIC	*Kepler*/K2/TESS ID	None
K2_campaign	K2 campaign number	None
GEDR3_source_id	*Gaia* EDR3 source ID	None
GEDR3_ra	*Gaia* EDR3 right ascension	deg
GEDR3_dec	*Gaia* EDR3 declination	deg
GEDR3_l	*Gaia* EDR3 galactic longitude	deg
GEDR3_b	*Gaia* EDR3 galactic latitude	deg
GEDR3_ecl_lon	*Gaia* EDR3 ecliptic longitude	deg
GEDR3_ecl_lat	*Gaia* EDR3 ecliptic latitude	deg
GEDR3_parallax	*Gaia* EDR3 parallax	mas
GEDR3_parallax_Z5	L21 correction (5p)	mas
GEDR3_phot_g_mean_mag	*Gaia* EDR3 G-band magnitude	mag
GEDR3_phot_bp_mean_mag	*Gaia* EDR3 G_{BP}-band magnitude	mag
GEDR3_phot_rp_mean_mag	*Gaia* EDR3 G_{RP}-band magnitude	mag
GEDR3_nu_eff_used_in_astrometry	*Gaia* EDR3 effective wavenumber	μm^{-1}
GEDR3_pseudocolour	*Gaia* EDR3 pseudocolour	μm^{-1}
GEDR3_astrometric_params_solved	*Gaia* EDR3 number of astrometric parameters solved	None
GEDR3_ruwe	*Gaia* EDR3 renormalised unit weight error	None
GEDR3_ipd_frac_multi_peak	*Gaia* EDR3 percent of successful-IPD windows with more than one peak	None
GEDR3_ipd_gof_harmonic_amplitude	*Gaia* EDR3 amplitude of the IPD GoF versus position angle of scan	None
GEDR3_ipd_frac_odd_win	*Gaia* EDR3 percent of transits with truncated windows or multiple gates	None
GEDR3_phot_bp_n_blended_transits	*Gaia* EDR3 number of BP blended transits	None
GEDR3_phot_rp_n_blended_transits	*Gaia* EDR3 number of RP blended transits	None
GEDR3_phot_bp_n_obs	*Gaia* EDR3 number of observations contributing to BP photometry	None
GEDR3_phot_rp_n_obs	*Gaia* EDR3 number of observations contributing to RP photometry	None
GEDR3_blending_fraction	*Gaia* EDR3 blending fraction	None
GEDR3_phot_bp_rp_excess_factor	*Gaia* EDR3 BP/RP excess factor	None
GEDR3_phot_bp_rp_excess_factor_corrected	*Gaia* EDR3 corrected BP/RP excess factor	None
GEDR3_phot_bp_rp_excess_factor_corrected_scatter	*Gaia* EDR3 1σ scatter for the corrected BP/RP excess factor	None
GDR3_non_single_star	*Gaia* DR3 flag indicating the availability in Non-Single Star tables	None
GDR3_distance_gspphot	*Gaia* DR3 distance from GSP-Phot	pc
GDR3_ag_gspphot	*Gaia* DR3 extinction in G-band from GSP-Phot	mag
2MASS_kmag	2MASS K_S -band magnitude	mag
APOGEE_ID	APOGEE ID	None
APOGEE_teff	APOGEE $T_{\rm eff}$	K
APOGEE_feh	APOGEE [Fe/H]	None
APOGEE_alpha	APOGEE [α/Fe]	None
APOGEE_mh	APOGEE [M/H]	None
APOGEE_ASPCAPFLAGS	APOGEE flag for issues associated with the ASPCAP fits	None
GALAH_teff	GALAH $T_{\rm eff}$	K
GALAH_feh	GALAH [Fe/H]	None
GALAH_alpha	GALAH [α/Fe]	None
GALAH_mh	GALAH [M/H]	None
GALAH_flag_sp	GALAH stellar parameter quality flag	None
GALAH_flag_fe_h	GALAH [Fe/H] quality flag	None
GALAH_flag_alpha_fe	GALAH [α/Fe] quality flag	None
MA09_numax	$\nu_{\rm max}$ from MA09 pipeline	μHz
MA09_Dnu	$\Delta\nu$ from MA09 pipeline	μHz
MA09_PARAM_mass	Mass from PARAM, based on MA09 and APOGEE/GALAH	$M_\odot$
MA09_PARAM_rad	Radius from PARAM, based on MA09 and APOGEE/GALAH	$R_\odot$
MA09_PARAM_mbol	Bolometric magnitude from PARAM, based on MA09 and APOGEE/GALAH	mag
MA09_PARAM_dist	Distance from PARAM, based on MA09 and APOGEE/GALAH	pc
MA09_PARAM_Av	Visual extinction from PARAM, based on MA09 and APOGEE/GALAH	mag
MA09_PARAM_Ks	K_S absolute magnitude from PARAM, based on MA09 and APOGEE/GALAH	mag
MA09_PARAM_parallax	Parallax from PARAM, based on MA09 and APOGEE/GALAH	mas
E20_numax	$\nu_{\rm max}$ from E20 pipeline	μHz
E20_Dnu	$\Delta\nu$ from E20 pipeline	μHz

Notes. There are four datasets in total: *Kepler*+ APOGEE, K2+ APOGEE, K2+ GALAH, and TESS+ APOGEE. In these tables we compile asteroseismic information from MA09 and E20, spectroscopic constraints from APOGEE DR17 (Abdurro'uf et al. 2022) or GALAH DR3 (Buder et al. 2021), and astrometric properties from *Gaia* (E)DR3 (Gaia Collaboration 2021, 2023). Where relevant, uncertainties defined either as the standard deviation ('err') or as the 16th or 84th percentiles (68L, 68U) are provided. For APOGEE we adopt conservative uncertainty values of 50 K and 0.05 dex for $T_{\rm eff}$ and [M/H], but keep the original values if they are larger. For GALAH, if [α/Fe] is not available, then the value and uncertainty on [M/H] are simply equal to those of [Fe/H]. GEDR3_blending_fraction, GEDR3_phot_bp_rp_excess_factor_corrected, GEDR3_phot_bp_rp_excess_factor_corrected_scatter are computed following Sect. 9.3 in Riello et al. (2021).

Table A.1. continued.

Column Identifier	Description	Units
`E20_PARAM_mass`	Mass from `PARAM`, based on E20 and APOGEE/GALAH	$M_\odot$
`E20_PARAM_rad`	Radius from `PARAM`, based on E20 and APOGEE/GALAH	$R_\odot$
`E20_PARAM_mbol`	Bolometric magnitude from `PARAM`, based on E20 and APOGEE/GALAH	mag
`E20_PARAM_dist`	Distance from `PARAM`, based on E20 and APOGEE/GALAH	pc
`E20_PARAM_Av`	Visual extinction from `PARAM`, based on E20 and APOGEE/GALAH	mag
`E20_PARAM_Ks`	K_S absolute magnitude from `PARAM`, based on E20 and APOGEE/GALAH	mag
`E20_PARAM_parallax`	Parallax from `PARAM`, based on E20 and APOGEE/GALAH	mas
`E17_evstate`	Elsworth et al. (2017) evolutionary state	None

Appendix B: Comparison with *Gaia* DR3 Apsis GSP-Phot distances

Figure B.1 compares distances from asteroseismology (based on E20 and APOGEE) and *Gaia* DR3 Apsis GSP-Phot for *Kepler*, K2, and TESS. As noted by Fouesneau et al. (2023), a good agreement is found to about 2 kpc; beyond this distance GSP-Phot tends to overestimate distances, as in *Kepler*, or on the contrary to systematically underestimate them at even further distances (see K2). No issues are found for TESS nearby targets.

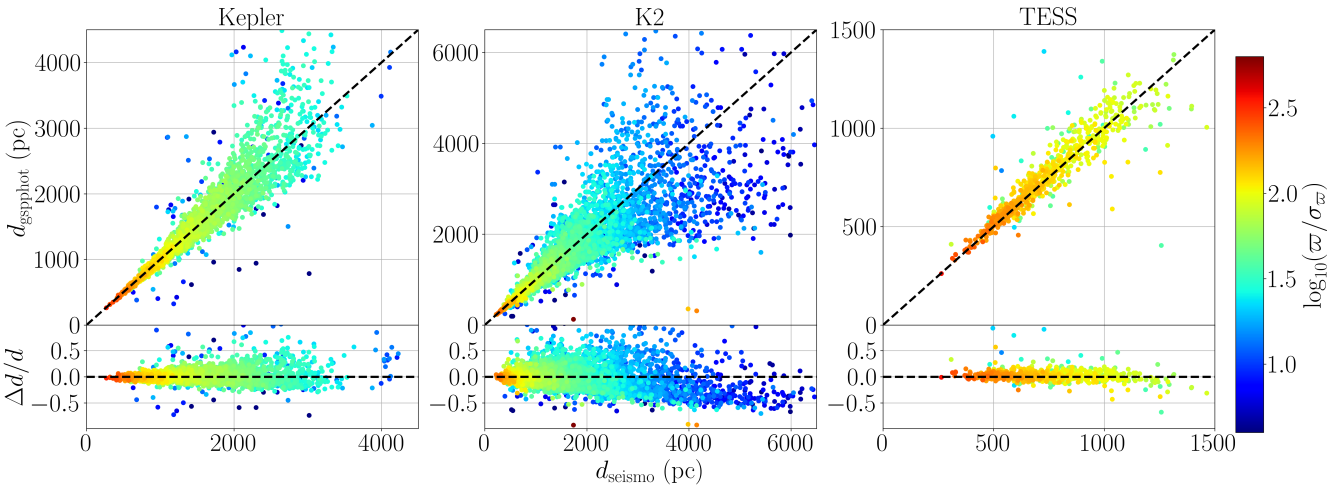

Fig. B.1. Comparison of *Gaia* DR3 Apsis GSP-Phot distances with asteroseismic values computed using E20 and APOGEE for *Kepler* (left), K2 (middle), and TESS (right). The bottom panels show the relative difference in distance. The colour scale indicates the *Gaia* parallax-to-error ratio. See Fig. 9 in Fouesneau et al. (2023) for a similar comparison with other asteroseismic datasets.

Appendix C: Parallax zero-point estimates from asteroseismology

Table C.1 gives a summary of the parallax offsets measured with the various combinations of asteroseismology and spectroscopy in the *Kepler*, K2 campaigns, and TESS fields.

Table C.1. Parallax zero points, measured as the difference between the *Gaia* EDR3 and the asteroseismic parallaxes ($\varpi_{\rm GEDR3} - \varpi_{\rm PARAM}$) for the asteroseismic fields considered in this study.

Field	MA09+APOGEE	E20+APOGEE *	MA09+GALAH	E20+GALAH
Kepler	−32.02 ± 0.36 (4687)	−20.09 ± 0.33 (4687)	-	-
K2 C01	−18.32 ± 3.00 (201)	−21.45 ± 3.00 (201)	−14.2 ± 2.93 (240)	−14.84 ± 2.87 (240)
K2 C02	−22.81 ± 2.11 (386)	−22.21 ± 2.28 (386)	−28.28 ± 1.81 (620)	−28.64 ± 1.89 (620)
K2 C03	−8.18 ± 2.05 (543)	−6.01 ± 2.07 (543)	−3.4 ± 2.82 (262)	−5.23 ± 2.88 (262)
K2 C04	−14.16 ± 1.42 (1092)	−18.30 ± 1.43 (1092)	−17.68 ± 2.48 (474)	−21.39 ± 2.55 (474)
K2 C05	−15.50 ± 1.41 (865)	−13.59 ± 1.46 (865)	−12.46 ± 1.65 (757)	−12.39 ± 1.65 (757)
K2 C06	−22.04 ± 1.56 (690)	−21.20 ± 1.60 (690)	−10.82 ± 2.72 (262)	−16.51 ± 2.53 (262)
K2 C07	−18.29 ± 1.91 (422)	−20.03 ± 1.99 (422)	−20.67 ± 1.42 (822)	−21.41 ± 1.46 (822)
K2 C08	−18.78 ± 2.24 (436)	−21.11 ± 2.35 (436)	−15.7 ± 4.0 (159)	−17.65 ± 3.89 (159)
K2 C10	−2.08 ± 3.59 (199)	−5.65 ± 3.49 (199)	−12.58 ± 4.07 (117)	−11.07 ± 3.99 (117)
K2 C11	−42.82 ± 3.56 (189)	−39.15 ± 3.66 (189)	−68.18 ± 4.79 (235)	−69.92 ± 4.81 (235)
K2 C12	2.49 ± 2.36 (462)	1.39 ± 2.22 (462)	−10.77 ± 6.5 (63)	−10.43 ± 6.43 (63)
K2 C13	−30.99 ± 2.03 (423)	−33.12 ± 2.06 (423)	−37.89 ± 2.03 (645)	−37.05 ± 1.99 (645)
K2 C14	−28.68 ± 2.65 (354)	−26.89 ± 2.41 (354)	−23.9 ± 4.00 (123)	−16.16 ± 4.04 (125)
K2 C15	−11.46 ± 13.08 (10)	−7.54 ± 11.21 (10)	−14.58 ± 1.78 (735)	−7.48 ± 1.62 (735)
K2 C16	−23.36 ± 2.60 (310)	−21.32 ± 2.52 (310)	−13.83 ± 3.29 (201)	−8.53 ± 3.16 (201)
K2 C17	−17.95 ± 2.32 (348)	−18.84 ± 2.42 (348)	−11.78 ± 3.81 (162)	−11.53 ± 3.66 (162)
K2 C18	−10.36 ± 5.27 (94)	−2.56 ± 5.55 (94)	4.08 ± 6.81 (78)	15.23 ± 6.35 (78)
TESS	−23.23 ± 1.27 (1253)	−41.43 ± 1.43 (1253)	-	-

Notes. Each column corresponds to a different combination of asteroseismic (MA09 or E20) and spectroscopic (APOGEE or GALAH) constraints. The offsets reported are given in μas, and the column used in Sects. 4 and 5 is followed by an asterisk. The number of stars is indicated in brackets. See Sect. 2 for more details about the samples.

Appendix D: Impact of L21 corrections on parallax offset estimation

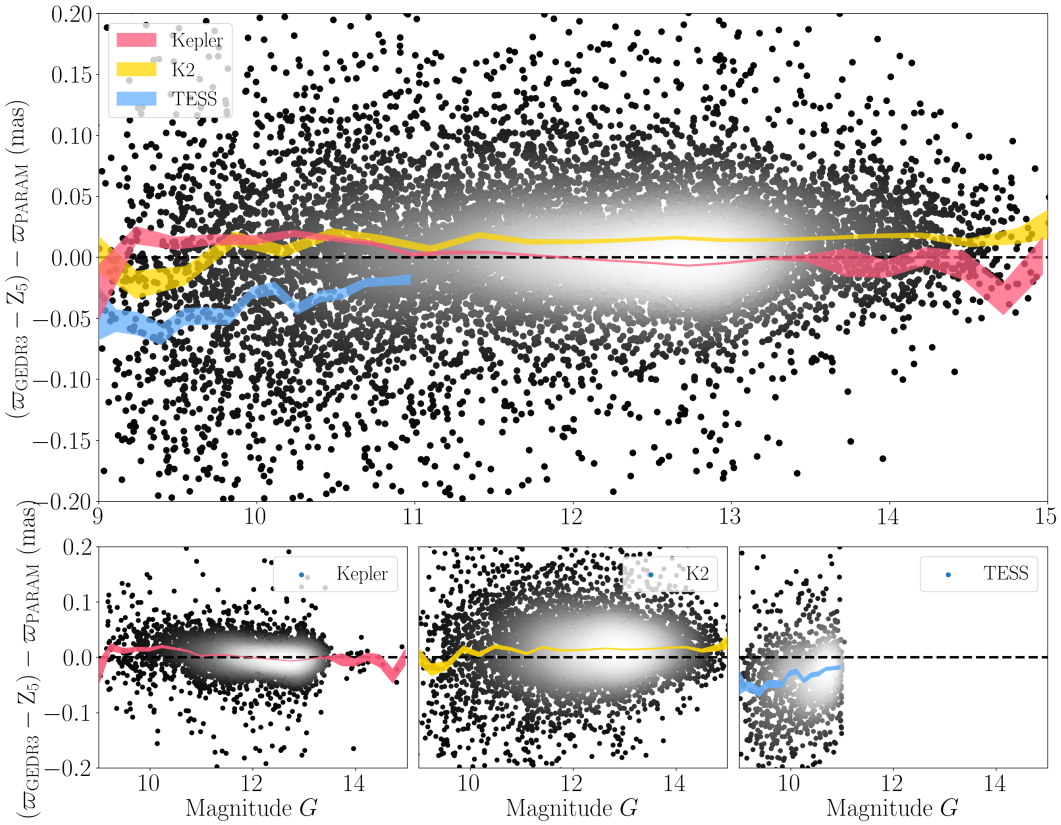

Fig. D.1. Same as Fig. 2, but including L21 corrections in the *Gaia* EDR3 parallaxes.